THE JOURNAL OF PHYSICAL CHEMISTRY C
A JOURNAL OF THE AMERICAN CHEMICAL SOCIETY

pubs.acs.org/JPCC

Article

Limited Ferromagnetic Interactions in Monolayers of MPS_3 (M = Mn and Ni)

Carmine Autieri, Giuseppe Cuono, Canio Noce, Milosz Rybak, Kamila M. Kotur, Cliò Efthimia Agrapidis, Krzysztof Wohlfeld, and Magdalena Birowska*

Cite This: *J. Phys. Chem. C* 2022, 126, 6791−6802

Read Online

ACCESS | Metrics & More | Article Recommendations | Supporting Information

ABSTRACT: We present a systematic study of the electronic and magnetic properties of two-dimensional ordered alloys, consisting of two representative hosts ($MnPS_3$ and $NiPS_3$) of transition metal phosphorus trichalcogenides doped with 3d elements. For both hosts, our DFT + U calculations are able to qualitatively reproduce the ratios and signs of all experimentally observed magnetic couplings. The relative strength of all antiferromagnetic exchange couplings, both in $MnPS_3$ and in $NiPS_3$, can successfully be explained using an effective direct exchange model: it reveals that the third-neighbor exchange dominates in $NiPS_3$ due to the filling of the t_{2g} subshell, whereas for $MnPS_3$, the first-neighbor exchange prevails, owing to the presence of the t_{2g} magnetism. On the other hand, the nearest neighbor ferromagnetic coupling in $NiPS_3$ can only be explained using a more complex superexchange model and is (also) largely triggered by the absence of the t_{2g} magnetism. For the doped systems, the DFT + U calculations revealed that magnetic impurities do not affect the magnetic ordering observed in the pure phases, and thus, in general in these systems, ferromagnetism may not be easily induced by such a kind of elemental doping. However, unlike for the hosts, the first and second (dopant−host) exchange couplings are of similar order of magnitude. This leads to frustration in the case of antiferromagnetic coupling and may be one of the reasons of the observed lower magnetic ordering temperature of the doped systems.

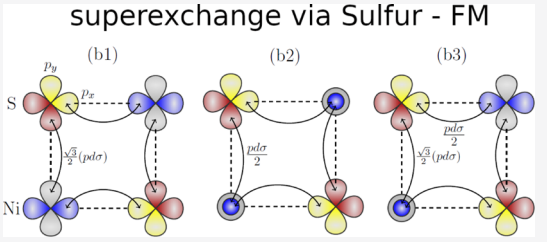

INTRODUCTION

Nonmagnetic van der Waals layered materials such as transition metal dichalcogenides have been extensively studied over the last several years.[1] Just recently, the intrinsic ferromagnetism in the true 2D limit has been reported,[2] initiating increasing excitement in the spintronics and 2D material communities. In particular, the long-range magnetic order has been observed for insulating CrI_3,[3] semiconducting $Cr_2Ge_2Te_6$,[4] and metallic Fe_3GeTe_2[5] compounds. In addition, topological spin structures have been predicted for 2D materials.[6]

Currently, the attention is on transition metal phosphorus trichalcogenides (MPX_3, where M stands for a transition atom and X = S and Se), which could be easily exfoliated down to monolayers[7,8] and are semiconducting materials with a wide range of band gaps.[9] The MPX_3 structures exhibit various antiferromagnetic (AFM) arrangements within the magnetic ions, which are theoretically expected to be measurable using different light polarizations.[10] Interestingly, the metal to insulator transition and superconductivity phase have been observed in this compound family.[11−13] In particular, the AFM insulator phase in bulk $FePS_3$ can be melted and transformed into the superconducting phase under high pressure, providing similarity to the high-T_c cuprate phase diagram.[14] In addition, theoretical predictions point to the existence of a large binding energy of excitons in $MnPS_3$, whereas the experimental reports have observed excitons in few layers of $NiPS_3$ strongly related to magnetic order.[13,15,16] Recent reports have demonstrated an all-optical control of the magnetic anisotropy in $NiPS_3$ by tuning the photon energy in resonance with an orbital transition between crystal field-split levels.[17] The aforementioned demonstrates that this family of compounds is an ideal platform to study correlation effects in the true 2D limit.

In contrast to ferromagnetic (FM) materials, the antiferromagnets exhibit limited applications, mostly in the terahertz regime as ultra-fast components or specialized embedded memory−logic devices.[18−20] Most of the current applications of magnetic crystals are based on the FM semiconductors, for which the band gap and FM order are crucial factors. The magnetic-phase transitions for the MPX_3 materials can be accomplished by applying stress,[21] changing the carrier concentration or applying voltage.[22] In addition, the "M" atoms in MPX_3 crystals might be substituted with other transition metal atoms inducing the FM order, as recently reported for a particular concentration of the non-magnetic

Received: January 26, 2022
Revised: March 30, 2022
Published: April 12, 2022

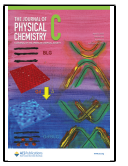

Downloaded via 93.40.228.211 on April 21, 2022 at 09:11:53 (UTC).
See https://pubs.acs.org/sharingguidelines for options on how to legitimately share published articles.

ACS Publications
© 2022 The Authors. Published by American Chemical Society

https://doi.org/10.1021/acs.jpcc.2c00646
J. Phys. Chem. C 2022, 126, 6791−6802

dopants in the $CrPSe_3$ host, resulting in a half-metallic FM state.[23] Moreover, a series of mixed systems in a bulk form[24−35] has been experimentally realized, thus entering a new playground of magnetic phases.

In addition, the magnetic and electronic properties of MPX_3 materials and critical Néel temperature (from T_N = 78 K for $MnPS_3$[36−38] up to T_N = 155 K for $NiPS_3$[36,37]) strongly depend on the type of magnetic ion in the host. Thus, an elemental substitution could be an efficient way to tune the magnetic properties of atomically thin layers, by changing the lattice parameters and magnetic moments. These quantities result in manipulation of the exchange interactions that could be an effective way to engineer highly functional materials, similar to magnetic heterostructures.[39] In particular, the main reason behind the idea that adding ions with the partially filled d-shells into the system might lead to the enhancement of the FM interactions is related to the so-called double-exchange mechanism:[40] the hopping between two correlated ions with different valences (and thus comparable Coulomb interactions) and relatively strong Hund's exchange is energetically favored provided that the spins on the neighboring ions are aligned in a parallel fashion. Such a mechanism might for instance be at play along the Cr−Mn bond: here the hopping from the manganese e_g orbitals (e_g^2 configuration) to the chromium e_g orbitals (e_g^1 configuration) lowers the total energy of the system provided that the spins on Cr and Mn are aligned ferromagnetically (for the antiparallel configuration, the strong Hund's exchange makes such a hopping energetically unfavorable). Note that such a double-exchange mechanism is similar to the one observed in the doped manganites which are FM—albeit here it is a bit more complex, for it involves two different magnetic ions (nevertheless, the latter should not be that important, for Cr and Mn have comparable values of the Coulomb interactions, *cf.* Table II of ref 41).

Altogether, in this work, we study the magnetic properties of the MPX_3 monolayers and try to understand (i) how FM interactions can be stabilized in these compounds and (ii) whether one can easily modify these compounds by elemental doping so that the FM interactions can be strengthened. To this end, we examine two representative hosts $MnPS_3$ and $NiPS_3$ in the undoped case and at a particular doping concentration of magnetic ions. Using first-principles calculations, we give qualitative and quantitative explanations of the origin of the exchange coupling strengths up to the third nearest neighbors and their respective ratios for $MnPS_3$ and $NiPS_3$ structures. Considering the model Hamiltonians with *ab initio* parametrization, we discuss the competition between the direct exchange and the superexchange mechanisms for the host structures. Next, we study various substantial sites of dopant atoms with mixed spins and mixed nearest-neighbor magnetic interactions. Here, again using first-principles calculations, we examine in detail the mixed exchange coupling parameters between the metal host and dopant atoms.

In the next section, we describe the computational details. In the third section, we will present our Results and Discussion while the last section is devoted to the Conclusions.

METHODS

DFT Computational Details. The first-principles calculations are performed in the framework of spin-polarized density functional theory (DFT) as is implemented in the VASP code.[42,43] The electron−ion interaction is modeled by using PAW pseudopotentials[44,45] with 3s and 3p states for P and S atoms and 3d and 4s states for Mn, Ni, and Cr being treated as valence states. The Perdew−Burke−Ernzerhof (PBE) exchange−correlation functional is employed.[46] The kinetic energy cutoff for the plane-wave expansion of the wave functions is set to 400 eV. A *k*-mesh of 10 × 6 × 2 is taken to sample an irreducible first Brillouin zone of the rectangular planar cell (see Figure S1 in Supporting Information) containing 20 atoms including four transition metal atoms. The lattice parameters have been fully optimized within the PBE + *U* approach for the magnetic ground state of the monolayers, assuming the rectangular supercell. In particular, the magnetic ground state (Hubbard *U* parameter) for $MnPS_3$ and $NiPS_3$ is AFM-N (*U* = 5 eV) and AFM-z (*U* = 6 eV), respectively. In the case of (2 × 2) supercell, which consists of four primitive hexagonal unit cells, the 5 × 5 × 1 *k*-mesh is chosen to obtain the optimized position of the atoms. Considering density of states (DOS) calculations, the denser *k*-mesh equal to 10 × 10 × 2 *k*-points is taken into account. The convergence criteria for the energy and force are set to 10^{-5} eV and 10^{-3} eV/Å, respectively. In order to properly model a monolayer system, 20 Å of a vacuum is added to neglect the spurious interaction between the image cells. Note that the standard exchange−correlation functionals are insufficient to account for a non-local nature of dispersive forces, which are crucial for layered materials and adsorption molecules on the surfaces.[47−50] Thus, the semi-empirical Grimme method[51] with a D3 parametrization is applied.[52] For the 2D materials, we can use the HSE for a better description of the gap;[53] however, in the case of magnetism also, GGA + *U* provides the same effect. We employ the GGA + *U* formalism proposed by Dudarev[54] to properly account for on-site Coulomb repulsion between 3d electrons of transition metal ions, by using effective Hubbard *U* parameters.

Note that the proper choice of the *U* values is not straightforward due to the lack of accurate experimental information on electronic properties. Also, the common choice to compare the band gaps obtained in DFT with experiments to judge the *U* values also need caution due to the fact that one-particle Kohn−Sham DOS cannot be directly compared to the measured data. Thus, we decided to compute the Hubbard *U* using the linear response method proposed by Cococcioni[55] for the monolayers of $MnPS_3$ and $NiPS_3$, and we obtained 5.6 eV for the Ni and 5.3 eV for the Mn. Therefore, we have used U_{Cr} = 4 eV, U_{Mn} = 5 eV, and U_{Ni} = 6 eV similar to the linear response results, which are typical *U* values reported for MPX_3 materials in previous reports.[21] Moreover, our Coulombic repulsions are close to the typical values of *U* in semiconductor compounds. Indeed, we find *U* = 6.4 for Ni^{2+} and *U* = 3.5 eV for Cr in oxides,[56] while the typical value of *U* for Mn^{2+} is *U* = 5 eV.[57,58]

To calculate the AFM direct exchange for $MnPS_3$ and $NiPS_3$, we extracted the real-space tight-binding Hamiltonian with atom-centered Wannier functions with d-like orbital projections on the transition metals using the Wannier90 code.[59,60] We calculated separately the hopping parameters for the orbitals, symmetric and antisymmetric with respect to the basal plane. The different symmetry and the separation in energy help to disentangle the two subsectors of the d manifold.[61,62] The calculation of the hopping parameters was carried out in the non-magnetic case to get rid of the magnetic effects and evaluate just the bare-band structure hopping parameters, and then, the hopping parameters will be used for the model Hamiltonian part.[63] In order to have parameters to use for the

https://doi.org/10.1021/acs.jpcc.2c00646
J. Phys. Chem. C 2022, 126, 6791−6802

model Hamiltonian, we do not perform the maximum localization so as to have the Wannier function basis of our tight-biding model as close as possible to the atomic orbitals.

RESULTS AND DISCUSSION

The results are presented as following: first, we present the results for the magnetic ground state of the hosts (pure $MnPS_3$ and $NiPS_3$ systems). In particular, we consider the exchange couplings within the DFT + U approach. Next, the AFM exchange mechanism is discussed within the minimal many-body model, and the AFM exchange coupling strengths are evaluated numerically using the Wannier basis with *ab initio* parametrization. Next, the qualitative explanation of the FM superexchange is presented. Finally, we present comprehensive studies of electronic and magnetic properties of benchmark alloys with a fixed concentration of dopants. The elemental substitution is employed at various atomic sites of the honeycomb lattice.

Undoped Hosts $MnPS_3$ and $NiPS_3$. *Magnetic Couplings within the DFT + U Approach.* The magnetic ground states of $MnPS_3$ and $NiPS_3$ exhibit AFM Néel (AFM-N)- and AFM zigzag (AFM-z)-type ordering (see Figure 1), respectively. The

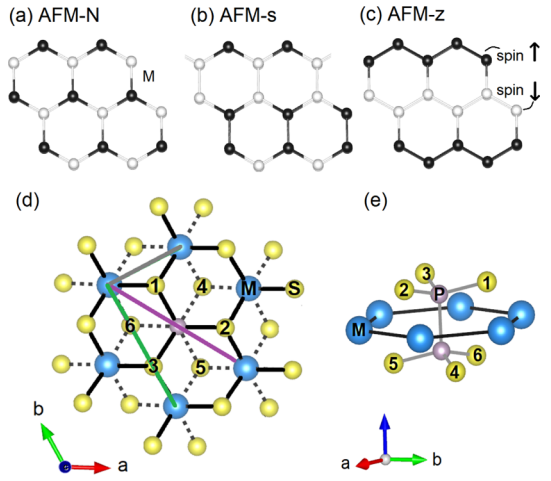

Figure 1. Spin arrangements of the metal atoms in (a) AFM Néel (AFM-N), (b) AFM stripy (AFM-s), and (c) AFM zigzag (AFM-z) states. (d) Top and (e) side views of the crystal structure of the MPX_3 system with the metal atoms denoted in blue and surrounded by the sulfur atoms (yellow balls). The gray, green, and violet lines indicate the NN, 2NN, and 3NN distance between the metal atoms, respectively. The dotted and solid lines indicate that the sulfur atoms are below and above the metal layer, respectively.

neutron diffraction data predicted that the Mn^{2+} ($3d^5$, $S = 5/2$) spins are slightly tilted (around 8°) from the perpendicular direction of the honeycomb lattice,[68] whereas the Ni^{2+} ($3d^8$, $S = 1$) spins are aligned within the honeycomb plane. In addition, due to the different filling of the 3d orbitals for various metals ions (Fe, Mn, Ni *etc.*), the size of the magnetic exchange coupling (J) also changes. The existence of magnetic ordering at finite temperature in 2D limit requires the magnetic anisotropy in accordance to the Mermin–Wagner theorem. Currently, only $FePS_3$, which possesses a strong out-of-plane easy axis, has been experimentally reported to exhibit AFM order in the monolayer up to 118 K.[8] In order to explain the anisotropic order, the dipolar interactions between the magnetic moments or a single-ion anisotropy resulting from a nonzero spin–orbit coupling should be considered. The recent experimental reports, such as magnon band measurements,[69] support the claim that the dipolar interactions should be the leading term, whereas the electron spin resonance[70] and critical behavior measurements[71] indicate that the single-ion anisotropy might come into play. In addition, experimental observations demonstrated that the AFM ordering persists down to bilayer samples and is suppressed in the monolayer.[72] Notably, the recent theoretical report[73] has questioned the Raman criterion used for the monolayer studies therein, suggesting that $NiPS_3$ magnetic ordering could be presented in monolayer samples, as also indicated by strong two-magnon continuum existing in thin samples of $NiPS_3$.[72] In the case of $MnPS_3$, the magnetic order has been presented down to the bilayer and was reported to be absent in the monolayer.[74] The suppression of the Néel temperature in thin samples can be associated with reducing the interplanar coupling in atomically thin samples.[3,72] Aforementioned results demonstrate that the magnetic ordering in monolayers of MPX_3 is still under a hot debate and many experiments are being carried out to verify the theoretical predictions. Similar effects of strong spin fluctuation and absence of interlayer exchange coupling that weaken the long-range spin order in the 2D limit have been reported in other layered magnets such as $Cr_2Ge_2Te_6$ and CrI_3.[3]

Here, we focus on the rationally invariant Heisenberg contribution, whereas the dipolar and single-ion contributions are out of the scope of the present work. The latter has been estimated to 0.3 and 0.009 meV for $NiPS_3$ and $MnPS_3$, respectively, and discussed theoretically in ref 66. Here, we present the results of exchange couplings up to the third nearest neighbor (for clarification, see Figure S1 in Supporting Information).

The exchange interaction up to the third nearest neighbor (J_i^M) between the metal atoms of the hosts has been widely studied in a series of previous studies[21,66,67,75−77] (see Table 1). Note that the prediction of the magnetic ground state within the DFT calculations does not depend on Hubbard interaction, whereas it is well known that the exchange coupling strength is sensitive to both U and the lattice parameters. We set the Hubbard U parameter to $U = 5$ eV and $U = 6$ eV for the 3d orbitals of Mn and Ni atoms, respectively. These values are calculated from first principles using the Cococcioni approach.[55] Our predicted J_i^M values are in good agreement with neutron diffraction experiments (see Table 1). The dominant exchange coupling is J_3^{Ni}, which is much stronger than J_1^{Ni}. Note, that the experimental ratio of critical temperatures $T_N^{MnPS_3}/T_N^{NiPS_3}$ is reflected in the relation of dominant contributions $J_3^{Ni} > J_1^{Mn}$. In both cases, J_2 is much smaller than the other two exchange couplings. In particular, J_2 and J_3 couplings might be considered as superexchange interactions involving the atoms in the path M–S1···S4–M for J_2 (see Figure 1d,e), where the S atoms are located in different sublayers, whereas the J_3 interaction is mediated by S atoms located in the same sublayer through the bridge M–S1···S2–M. One could expect stronger hybridization of the S p states and M 3d states within the same sublayer of S atoms. In addition, the calculations reveal that J_1 is AFM and FM for $MnPS_3$ and $NiPS_3$, respectively. Note that for both $MnPS_3$ and $NiPS_3$, the angle between the M–S–M atoms is close to 90° (83.4° for $MnPS_3$ and 85.4° for $NiPS_3$) for pointing to FM superexchange according to Goodenough–Kanamori–Ander-

https://doi.org/10.1021/acs.jpcc.2c00646
J. Phys. Chem. C 2022, 126, 6791−6802

Table 1. Exchange Coupling Strengths J_i^M of $MnPS_3$ and $NiPS_3$ Systems Using Model Calculations and Various Lattice Parameters and On-Site Coulomb Repulsion U in the DFT + U Calculations[a]

structure	J_1^M	J_2^M	J_3^M	$\lvert J_2^M/J_1^M\rvert$	$\lvert J_3^M/J_1^M\rvert$
$MnPS_3$ (model calculations, see caption above)	19.5	0.35	7.76	0.02	0.40
$MnPS_3$ (PBE, a = 6.00 Å, AFM-N)[66]	1.21	0.18	0.54	0.15	0.45
$MnPS_3$ (U = 5 eV, a = 6.11 Å, AFM-N) this work	1.04	0.05	0.53	0.05	0.51
$MnPS_3$ (U = 5 eV, a = 5.88 Å, AFM-N)[67]	1.58	0.08	0.46	0.05	0.29
$MnPS_3$ (U = 4 eV, a = 6.00 Å, AFM-N)[21]	0.4	0.03	0.15	0.08	0.38
$MnPS_3$ (U = 3 eV, a = 6.00 Å, AFM-N)[66]	1.42	0.08	0.52	0.06	0.37
$MnPS_3$ (experiment, AFM-N)[64]	1.54	0.14	0.36	0.09	0.23
$NiPS_3$ (model calculations, see caption above)	−4.9	0.06	14.8	0.01	3.0
$NiPS_3$ (PBE, a = 5.78 Å, AFM-z)[21]	−11.3	−0.12	36	0.01	3.2
$NiPS_3$ (U = 6 eV, a = 5.84 Å, AFM-z) this work	−3.34	−0.19	13.7	0.06	4.1
$NiPS_3$ (U = 4 eV, a = 5.78 Å, AFM-z)[21]	−4.11	1.95	17.4	0.47	4.2
$NiPS_3$ (U = 3 eV, a = 5.78 Å, AFM-z)[66]	−2.6	−0.32	14	0.12	5.4
$NiPS_3$ (experiment, AFM-z)[65]	−3.8	0.2	13.8	0.05	3.6

[a]Positive (negative) J_i^M indicate AFM (FM) correlations, respectively. Note, that in refs 64 and 65, different conventions of the exchange couplings J_i^M were used. The AFM-N and AFM-z indicate the magnetic ground state of the system. The exchange couplings in the model calculations are obtained within the direct exchange mechanism [for $MnPS_3$ using eqs 2 and 4 whereas for $NiPS_3$ using eq 3]—except for J_1^{Ni} for $NiPS_3$, which contains also an important superexchange contribution and follows from eq 7; see text for further details. More details on the calculation of the magnetic exchanges within the DFT + U approach are present in Supporting Information. All values are given in meV.

son rules.[78,79] The direct M−M and indirect M−S−M (superexchange) mechanisms are of crucial importance to understand the differences between these two systems.

Effective Direct Exchange and AFM Couplings. In order to understand the origin of the exchange couplings and their relative strengths, we consider model Hamiltonians for the direct and superexchange interactions. Note, that the direct exchange discussed in this work is a (second order) kinetic exchange process, which involves only the hopping between the transition metal ions, with the ligands not explicitly involved, *cf.* ref 80, whereas a superexchange term is a fourth- (or higher-) order kinetic exchange process, which explicitly involves the hopping over the ligands, *cf.* ref 80. In addition, we are pointing out below the mechanisms which could impact the sign of J_1.

To understand the origin of the magnetic couplings, we first write down a minimal many-body model which solely contains the valence electrons of the transition metal ion[81]—the multiband Hubbard model. From this, using the second-order perturbation theory that is valid in the Mott insulating limit, we derive the (effective) direct exchange processes. By construction, all obtained spin couplings have to be AFM. Therefore, while surprisingly successful, the following simple analysis will not be able to explain the onset of the FM couplings in $NiPS_3$ (more on this at the end of the section).

In the monolayers of $MnPS_3$ and $NiPS_3$, the metal atoms are surrounded by six sulfur atoms (MS_6 octahedron) and exhibit D_{3d} point group symmetry in trigonal anti-prismatic environment of the ligands (sulfur atoms), see Figure 2a. Hence, due to this trigonal crystal field effect, the d manifold splits in two disentangled subsets of bands. The only coupling between these subsets is the spin−orbit coupling.[82] The bands lower in energy are even ($d_{x^2-y^2}$, d_{xy}, and d_{z^2}) with respect to the basal plane, while the bands higher in energy are odd (d_{xz} and d_{yz}) with respect to the basal plane. The Mn ion is d^5 and Mn d bands split into half-filled even and half-filled odd bands; therefore, the magnetic coupling acquires contributions both from the even and the odd orbitals. Instead, because the Ni ion has a d^8 configuration, the even orbitals are fully occupied, and therefore, there is no magnetic contribution from these

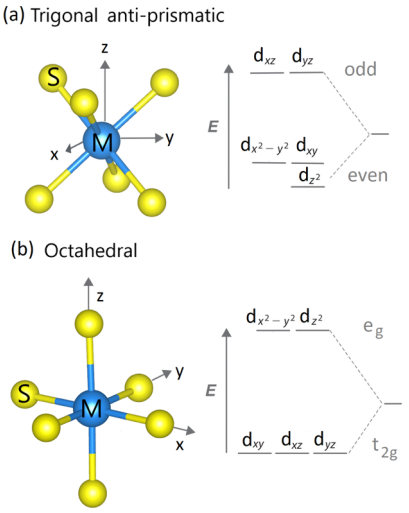

Figure 2. (a) Trigonal anti-prismatic and (b) octahedral geometries. On the right side, the d-orbital splitting of the metal atom in the corresponding crystal fields is shown. M and S denote the metal atom and sulfur atom, respectively.

orbitals. Altogether, the minimal model is the five-band Hubbard model with a simplified structure of the Coulomb interactions (no spin on-site spin exchange and pair-hopping terms, *cf.* ref 83)

$$H = \sum_{im\sigma}\sum_{i'm'\sigma'} t_{m,m}^{i,i'} u_{\sigma,\sigma'}^{i,i'} c_{im\sigma}^{\dagger} c_{i'm'\sigma'} + U\sum_{im} n_{im\uparrow}n_{im\downarrow} + \frac{1}{2}\sum_{im(\neq m')\sigma\sigma'} (U - 2J_H - J_H\delta_{\sigma,\sigma'})n_{im\sigma}n_{im'\sigma'} \quad (1)$$

In this model, $c_{im\sigma}^{\dagger}$ creates an electron with spin $\sigma = \uparrow, \downarrow$ in a Wannier orbital $|m\rangle = |x^2 - y^2\rangle, |xy\rangle, |xz\rangle, |yz\rangle$, or $|3z^2 - r^2\rangle$ at site i, and $n_{im\sigma} = c_{im\sigma}^{\dagger}c_{im\sigma}$. $\uparrow$ ($\downarrow$) indicates the spin up (down). The parameter $t_{m,m'}^{i,i'}$ is the hopping integral from orbital m at site i to orbital m' at site i'. The on-site terms $t_{m,m'} = \varepsilon_{m,m'}$ give the crystal field splitting. U and J_H are the direct and (Hund) exchange terms of the screened on-site Coulomb interaction.

https://doi.org/10.1021/acs.jpcc.2c00646
J. Phys. Chem. C 2022, 126, 6791−6802

We applied second-order perturbation theory in t/U and for the commensurate electron filling of Mn and Ni ions. The direct exchange constant for the valence electrons occupying the Mn odd orbitals is

$$J_{i,i'}^{\mathrm{Mn,odd}} \sim \frac{2(|t_{a,a}^{i,i'}|^2 + |t_{b,b}^{i,i'}|^2) + |t_{a,b}^{i,i'}|^2 + |t_{b,a}^{i,i'}|^2}{U^{\mathrm{Mn}} + 4J_{\mathrm{H}}^{\mathrm{Mn}}} \tag{2}$$

where a and b are the dxz and d_{yz} orbitals, respectively, while i and i' are the Mn lattice sites. In this formula, we take in consideration both the cases with $i = 1 \neq i' = 2$ and $i = i' = 1$. U^{Mn} and $J_{\mathrm{H}}^{\mathrm{Mn}}$ are the Coulomb repulsion and Hund coupling, respectively, in the case of the Mn atoms. The Hund's rule interaction between odd and even electrons yields a magnetic coupling between these electrons; therefore, the denominator depends on the occupancy of the even orbitals. By symmetry, the on-site energies are $\epsilon_a^{\mathrm{Mn1}} = \epsilon_a^{\mathrm{Mn2}} = \epsilon_b^{\mathrm{Mn1}} = \epsilon_b^{\mathrm{Mn2}}$.

Similarly, we obtain the direct exchange constant for the valence electrons occupying the odd orbitals of the Ni atoms

$$J_{j,j'}^{\mathrm{Ni,odd}} \sim \frac{2(|t_{a,a}^{j,j'}|^2 + 2|t_{b,b}^{j,j'}|^2) + |t_{a,b}^{j,j'}|^2 + |t_{b,a}^{j,j'}|^2}{U^{\mathrm{Ni}} + J_{\mathrm{H}}^{\mathrm{Ni}}} \tag{3}$$

where a and b are the d_{xz} and d_{yz} orbitals, respectively, while j, j' are the Ni lattice sites. In this formula, we take in consideration both the cases with $j = 1 \neq j' = 2$ and $j = j' = 1$. U^{Ni} and $J_{\mathrm{H}}^{\mathrm{Ni}}$ are the Coulomb repulsion and Hund coupling, respectively, in the case of the Ni atoms. By symmetry the on-site energies are $\epsilon_a^{\mathrm{Ni1}} = \epsilon_a^{\mathrm{Ni2}} = \epsilon_b^{\mathrm{Ni1}} = \epsilon_b^{\mathrm{Ni2}}$.

Finally, the direct exchange constant for the even Mn orbitals is as follows

$$\begin{aligned} J_{i,i'}^{\mathrm{Mn,even}} \sim{}& \frac{2(|t_{c,c}^{i,i'}|^2 + |t_{d,d}^{i,i'}|^2 + |t_{e,e}^{i,i'}|^2) + |t_{d,e}^{i,i'}|^2 + |t_{e,d}^{i,i'}|^2}{U^{\mathrm{Mn}} + 4J_{\mathrm{H}}^{\mathrm{Mn}}} \\ &+ \frac{|t_{c,d}^{i,i'}|^2}{U^{\mathrm{Mn}} + 4J_{\mathrm{H}}^{\mathrm{Mn}} + \epsilon_d^{i'} - \epsilon_c^{i}} + \frac{|t_{d,c}^{i,i'}|^2}{U^{\mathrm{Mn}} + 4J_{\mathrm{H}}^{\mathrm{Mn}} + \epsilon_c^{i'} - \epsilon_d^{i}} \\ &+ \frac{|t_{c,e}^{i,i'}|^2}{U^{\mathrm{Mn}} + 4J_{\mathrm{H}}^{\mathrm{Mn}} + \epsilon_e^{i'} - \epsilon_c^{i}} + \frac{|t_{e,c}^{i,i'}|^2}{U^{\mathrm{Mn}} + 4J_{\mathrm{H}}^{\mathrm{Mn}} + \epsilon_c^{i'} - \epsilon_e^{i}} \end{aligned} \tag{4}$$

where c, d and e are the orbitals d_{z^2}, $d_{x^2-y^2}$, $d_{x,y}$ respectively, while i and i' are the metal lattice sites. In this formula, we take in consideration both the cases with $i = 1 \neq i' = 2$ and $i = i' = 1$. U^{Mn} and $J_{\mathrm{H}}^{\mathrm{Mn}}$ are the Coulomb repulsion and Hund coupling, respectively, in the case of the Mn atoms. By symmetry the on-site energies are $\epsilon_c^{\mathrm{Mn1}} = \epsilon_c^{\mathrm{Mn2}}$ and $\epsilon_d^{\mathrm{Mn1}} = \epsilon_d^{\mathrm{Mn2}} = \epsilon_e^{\mathrm{Mn1}} = \epsilon_e^{\mathrm{Mn2}}$.

The obtained (total) direct exchange, $J = J^{\mathrm{odd}} + J^{\mathrm{even}}$, is positive for both Mn and Ni ion and for any distance $j - j'$. Hence, as already mentioned, it is always AFM by construction.

Numerical Evaluation of the AFM Couplings. The Wannier basis provides us with *ab initio* values of the hopping integrals and crystal field splitting. We calculate the hopping parameters and the on-site energies using the interpolated band structure of the Wannier functions of the d-subsector. The on-site energies for Mn and Ni are: $\epsilon_a^{\mathrm{Mn1}} = -1197.7$ meV, $\epsilon_c^{\mathrm{Mn1}} = -2082.6$ meV, $\epsilon_d^{\mathrm{Mn1}} = -2179.3$ meV, and $\epsilon_a^{\mathrm{Ni1}} = -1768.5$ meV. We have three first nearest neighbors (1NN), six second nearest neighbors (2NN), and three third nearest neighbors (3NN). In the case of odd orbitals, the 3NN couplings are greater than the 1NN couplings, even by an order of magnitude; therefore, it is very important to consider these hopping amplitudes in the calculations. On the other hand, for even orbitals, the 1NN couplings are greater than the 3NN couplings. The 2NN couplings are always smaller with respect to the 1NN couplings and 3NN couplings. In the case of even orbitals, we neglect the difference between the on-site energies assuming the following approximation $\epsilon_c^{\mathrm{Mn}} - \epsilon_d^{\mathrm{Mn}}$, $\epsilon_c^{\mathrm{Mn}} - \epsilon_e^{\mathrm{Mn}} \ll (U^{\mathrm{Mn}} + 4J_{\mathrm{H}}^{\mathrm{Mn}})$.

Now, we will numerically evaluate the second- and third-neighbor direct exchange as a function of the first-neighbor direct exchange. For the odd subsector of $MnPS_3$, we obtain $J_2^{\mathrm{Mn,odd}} = 0.037J_1^{\mathrm{Mn,odd}}$ and $J_3^{\mathrm{Mn,odd}} = 2.026J_1^{\mathrm{Mn,odd}}$. For the even subsector of the $MnPS_3$, we obtain $J_2^{\mathrm{Mn,even}} = 0.015J_1^{\mathrm{Mn,even}}$ and $J_3^{\mathrm{Mn,even}} = 0.016J_1^{\mathrm{Mn,even}}$. Considering that $J^{\mathrm{Ni,even}} = 0$ due to fully occupied even orbitals, for the odd subsector of $NiPS_3$, we obtain $J_2^{\mathrm{Ni,odd}} = 0.047J_1^{\mathrm{Ni,odd}}$ and $J_3^{\mathrm{Ni,odd}} = 11.09J_1^{\mathrm{Ni,odd}}$. If we consider the total direct exchange value as the sum of the odd and even sector, we have $J_1^{\mathrm{Mn}} = (152.4\ \mathrm{eV{\cdot}meV})/(U^{\mathrm{Mn}} + 4J_{\mathrm{H}}^{\mathrm{Mn}})$ for the first-neighbor coupling in $MnPS_3$. For the second and third neighbors, we obtain $J_2^{\mathrm{Mn}} = 0.018J_1^{\mathrm{Mn}}$ and $J_3^{\mathrm{Mn}} = 0.397J_1^{\mathrm{Mn}}$, and therefore, for $MnPS_3$, the dominant direct exchange comes from the first-neighbor coupling. Using a Coulomb repulsion of 5 eV for Mn and a Hund coupling of 0.7 eV, we obtain the numerical values equal to $J_1^{\mathrm{Mn}} = 19.5$ meV, $J_2^{\mathrm{Mn}} = 0.35$ meV, and $J_3^{\mathrm{Mn}} = 7.76$ meV, (see Table 1). Note that the values are overestimated in comparison to experimental values (see Table 1); however, the signs and the dominant contributions are the same.

When we numerically evaluate the direct exchange of $NiPS_3$, we obtain $J_1^{\mathrm{Ni}} = (8.957\ \mathrm{eV{\cdot}meV})/(U^{\mathrm{Ni}} + J_{\mathrm{H}}^{\mathrm{Ni}})$ for the first-neighbor coupling, $J_2^{\mathrm{Ni}} = 0.047J_1^{\mathrm{Ni}}$ and $J_3^{\mathrm{Ni}} = 11.09J_1^{\mathrm{Ni}}$ for the second and third neighbors, respectively. Remarkably, the 3NN magnetic direct exchange is larger than the 1NN exchange in the odd case. Using a Coulomb repulsion of 6 eV for Ni and a Hund coupling of 0.7 eV, we obtain the numerical values equal to $J_1^{\mathrm{Ni}} = 1.3$ meV, $J_2^{\mathrm{Ni}} = 0.06$ meV, and $J_3^{\mathrm{Ni}} = 14.8$ meV, where last two are reported in Table 1. Note, that J_2^{Ni} and J_3^{Ni} are in good agreement with experimental values (see Table 1), while J_1^{Ni} is significantly different and has a wrong sign. Therefore, in the case of J_1^{Ni}, a more complex superexchange model will be presented further in the text.

Altogether, we obtain that the simple direct exchange scheme gives $J_3^{\mathrm{Ni}} \gg J_1^{\mathrm{Ni}} \gg J_2^{\mathrm{Ni}}$ and $J_1^{\mathrm{Mn}} > J_3^{\mathrm{Mn}} \gg J_2^{\mathrm{Mn}}$. In the Ni case, the leading term is J_3^{Ni}, while in the Mn case, the leading term is J_1^{Mn}. The reason for this different behavior comes from the different filling that produces $J^{\mathrm{Ni,even}} = 0$. The calculated direct exchange couplings are qualitatively in agreement with the magnetic couplings obtained experimentally or using DFT—except that J_1^{Ni} and J_2^{Ni} are FM due to more complex magnetic exchange not taken into account by the (simple) direct exchange scheme (see below). Even though the latter coupling is relatively small, note that considering in more detail, such discrepancy is relevant for an accurate description of the magnetic coupling and, hence, of the magnetic critical temperature. The different leading exchange terms in Mn and Ni compounds open the way to manipulate the magnetism by tuning the concentration of Mn and Ni compounds or by adding new magnetic materials as dopants.

Superexchange and FM Coupling in $NiPS_3$. So far, we considered an effective direct exchange model, which solely contained the exchange processes due to the electrons hopping between the transition metal (Mn or Ni) ions. Note that such a model should be considered an effective one, for in reality, the

https://doi.org/10.1021/acs.jpcc.2c00646
J. Phys. Chem. C 2022, 126, 6791−6802

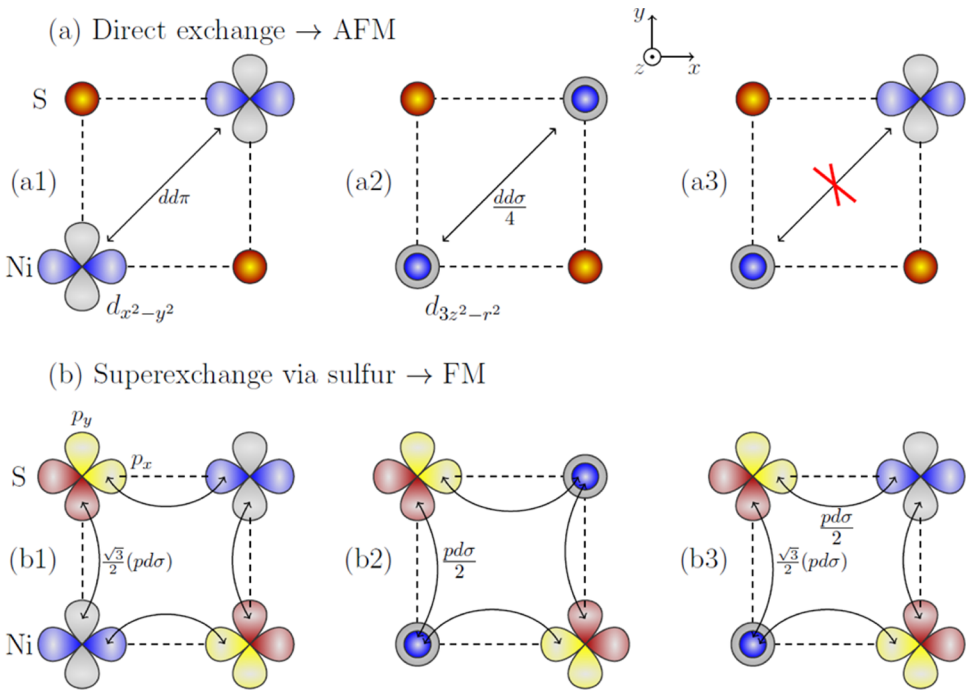

Figure 3. Schematic comparison between the AFM direct exchange (top panels) and the FM superexchange (bottom panels) processes in $NiPS_3$. Finite direct-AFM exchange processes due to (a1) nonzero hopping elements $\propto dd\pi$ between the nearest-neighbor $d_{x^2-y^2}$ orbitals on nickel and (a2) nonzero hopping elements $\propto dd\sigma$ between the nearest-neighbor $d_{3z^2-r^2}$ orbitals on nickel. Lack of direct-AFM exchange processes due to vanishing hopping elements between the nearest-neighbor $d_{x^2-y^2}$ and $d_{3z^2-r^2}$ on nickel. Finite FM superexchange processes due to (b1) nonzero hopping elements $\propto pd\sigma$ between the nearest-neighbor $d_{x^2-y^2}$ orbitals on nickel and the nearest-neighbor p_x/p_y orbital on sulfur, (b2) nonzero hopping elements $\propto pd\sigma$ between the $d_{3z^2-r^2}$ orbitals on nickel and the nearest-neighbor p_x/p_y orbital on sulfur, and (b3) nonzero hopping elements $\propto pd\sigma$ between the $d_{x^2-y^2}$ orbital on nickel and the nearest-neighbor p_x/p_y orbital on sulfur and the $d_{3z^2-r^2}$ orbital on nickel and the nearest-neighbor p_x/p_y orbital on sulfur. See text for more details.

hopping between the neighboring Mn or Ni ions is predominantly mediated by the sulfur ions. Hence, a natural extension of the direct exchange model should explicitly contain the exchange processes on the sulfur ions—in fact, it is such a nearest neighbor superexchange model[84] that is studied below to explain the onset of the nearest neighbor FM exchange in $NiPS_3$. Note that for consistency, we comment at the end of this subsubsection why the more complex superexchange model is not needed to understand the other, the first- and third-neighbor,[a] magnetic couplings in MPS_3—that is, the effective direct exchange model is enough.

We introduce the nearest neighbor superexchange model[84] for $NiPS_3$ by considering two Ni ions connected *via* two sulfur atoms over two 90° bonds, see Figure 3. Note that, because Ni^{2+} is in a d^8 configuration and sulfur ions are fully occupied, it is easier to consider the hole language as discussed below. Moreover, in what follows, we neglect the small trigonal distortions and we assume an octahedral crystal field with the division in t_{2g} and e_g orbitals [with the coordinate system defined in such a way that the *xy* plane coincides with the plane formed by the nearest-neighbor transition metal ion and sulfur, see Figures 2b and 3]. Hence, we begin by considering a fully atomic limit without hopping (zeroth order of perturbation theory in the small kinetic energy) in which there are two holes localized in two distinct Ni e_g orbitals ($d_{x^2-y^2}$, $d_{3z^2-r^2}$; in what follows assumed to be energetically degenerate, see also above) and two (lying higher by the charge transfer energy Δ) empty p orbitals (p_x, py) on sulfur. As before, due to the strong Hund's rule J_H, the two Ni^{2+} holes form a high spin $S = 1$ state. Now, let us perform a perturbation theory in the kinetic energy (over Coulomb repulsion U and charge transfer energy Δ) and consider the possible exchange processes—which are of two kinds:

First, there are direct exchange processes between the nickel ions, see Figure 3a. By definition, these concern virtual occupancies of one of the nickel ions by three holes [with a relative energy cost of $U + J_H$ according to the simplified structure of the Coulomb interactions, see eq 1] and are possible once the hole can directly hop back and forth between the nickel orbitals under consideration. According to the Slater−Koster scheme,[85] which is qualitatively confirmed by our DFT calculations, the latter is allowed between the pair of $d_{x^2-y^2}$ orbital ($dd\pi$ hopping element) and between the pair of $d_{3z^2-r^2}$ orbitals ($dd\sigma/4$ hopping element; the small $dd\delta$ element can be neglected), *cf.* Figure 3(a1,a2); note that the hopping between the $d_{x^2-y^2}$ and the $d_{3z^2-r^2}$ orbital vanishes in this geometry, *cf.* Figure 3(a3). Altogether we obtain the nearest-neighbor direct exchange contribution

$$J_1^{\mathrm{Ni,direct}} = 4\left[\frac{(dd\pi)^2}{U+J_H} + \frac{(dd\sigma/4)^2}{U+J_H}\right] \approx 4\frac{(dd\pi)^2}{U+J_H} \qquad (5)$$

where we assumed a typical relation between the Slater−Koster hopping integrals $dd\sigma \approx 2dd\pi$. It is important to state here that the above direct exchange process is different than the *effective* direct exchanges process defined in the previous subsections—for the latter ones may include all indirect hoppings (*e.g., via* sulfur) between the two nearest neighbor nickel ions.

Second, there are superexchange processes between the nickel ions, see Figure 3b. By definition these concern virtual

https://doi.org/10.1021/acs.jpcc.2c00646
J. Phys. Chem. C 2022, 126, 6791−6802

occupancies of one of the sulfur ions by two holes (with an energy cost associated with the charge transfer 2Δ for antiparallel spins or $2\Delta - J_H$ for parallel spins[b]) and are possible once the two holes hop back and forth between the sulfur and nickel orbitals under consideration. Again, using the Slater–Koster scheme,[85] and considering the three distinct possible hopping processes shown in Figure 3(b1–b3), we obtain the nearest neighbor superexchange contribution

$$J_1^{\mathrm{Ni,SE}} = \frac{1}{2}\left(\frac{4}{2\Delta} - \frac{4}{2\Delta - J_H}\right) \times \left[\left(\frac{\sqrt{3}\,pd\sigma}{2}\right)^2\left(\frac{\sqrt{3}\,pd\sigma}{2}\right)^2\frac{2}{\Delta^2} + \left(\frac{pd\sigma}{2}\right)^2\left(\frac{pd\sigma}{2}\right)^2\frac{2}{\Delta^2} + \left(\frac{\sqrt{3}\,pd\sigma}{2}\right)^2\left(\frac{pd\sigma}{2}\right)^2\frac{4}{\Delta^2}\right]^2 = -2J_H\frac{(pd\sigma)^4}{(2\Delta - J_H)\Delta^3} \quad (6)$$

which is negative (FM) due to the lowering of the energy for a FM (virtual) occupancy of sulfur by two holes in the superexchange process. Note that for a given Ni–Ni bond, there are always two superexchange processes: one over the top-left and one over the bottom-right sulfur (hence the factor of two within the square brackets in the above formula). Moreover, the process depicted in Figure 3(b3) has to be multiplied by a factor of two, for one can interchange the position of the $d_{x^2-y^2}$ and the $d_{3z^2-r^2}$ orbital and in this way double the amplitude of this process. Finally note that, due to the fact that we have spins $S = 1$ on nickel, overall the above superexchange process is reduced by a factor 1/2 with respect to to an analogous one for the $S = 1/2$ on copper (the superexchange processes have to be projected on the high-spin $S = 1$ states on both nickel ions—hence a factor of $(1/\sqrt{2})^2$ reduction).

Let us now comment why the above FM superexchange mechanism is not important for the nearest neighbor exchange in $MnPS_3$. The reason for this is that in the case of manganese ions, we are a bit closer to the situation discussed in ref 84, which, for instance, shows the AFM exchange coupling in the case of half-filled t_{2g} subshells of Cr^{3+} in $LiCrS_2$. More precisely, the situation for the Mn^{2+} ions is as follows. On one hand, the AFM direct exchange is much stronger for Mn^{2+} because one of the t_{2g} electrons (the d_{xy}) can hop over the $dd\sigma$ bond. On the other hand, the superexchange also contains an additional strong[84] AFM contribution due to the superexchange processes over one p_z sulfur orbital—which strongly hybridizes with the two nearest t_{2g} orbitals. Altogether, as confirmed by the effective direct exchange studies in the previous subsection, these two mechanisms originating in the t_{2g} exchange processes easily overcome the (above-described) FM processes for the e_g orbitals.

Finally, we mention that the (surprisingly) strong third-neighbor coupling in MPS_3 can easily be explained using the superexchange model. First, for the t_{2g} sector, the strong AFM third-neighbor coupling is already discussed in ref 84—see Figure 7 of the reference. Second, one can easily imagine that a similarly strong AFM coupling can also be realized for the e_g electrons: in order to understand it, one just needs to replace the two third-neighbor d_{xy} orbitals with the $d_{x^2-y^2}$ orbitals and rotate the sulfur p orbitals by 90° in the process shown in Figure 7 of ref 84. In fact, the latter one should have a very high amplitude and hence a really strong third-neighbor exchange in $NiPS_3$.

Numerical Evaluation of the FM Coupling in $NiPS_3$. Having derived the direct exchange and superexchange processes between the nearest neighbor nickel ions, we are now ready to estimate the contributions of these both (competing) spin interaction terms. To this end, we assume that Coulomb repulsion $U = 6$ eV (the chosen value of our DFT + U approach, see Table 1) and take a typical (for 3d transition metal compounds) value of Hund's exchange $J_H = 0.7$ eV. Next, based on the DFT calculations, we estimate that (i) the charge transfer energy $\Delta = 3$ eV, (ii) the hopping $pd\sigma = 0.9$ eV, and (iii) the hopping $dd\sigma = 0.05$ eV. From this and using eqs 5 and 6, we can easily calculate the AFM and FM contributions to the spin exchange

$$J_1^{\mathrm{Ni,direct}} \approx 1.5\ \mathrm{meV},\quad J_1^{\mathrm{Ni,SE}} \approx -6.4\ \mathrm{meV} \quad (7)$$

As the second exchange is larger (by absolute value), we conclude that it is a relatively strong superexchange along the 90° nickel-sulfur-nickel bonds, which triggers the FM exchange along the nearest neighbor nickel ions. The sum of the aforementioned contributions leads to FM exchange coupling ($J_1^{\mathrm{Ni}} = -4.9$), which is in good agreement with experimental studies (see Table 1).

At this point, we would like to comment on the fact that for the edge-sharing copper chains, typically one entirely neglects the direct exchange *cf.* ref 86. The reason for this is that, in the copper chains, the direct copper hopping $dd\sigma = 0.08$ eV,[87] whereas usually one assumes that for the cuprates, $pd\sigma \approx 1.5$ eV. With such hopping parameters (and assuming the typical cuprate values of $U = 8$ eV, $\Delta = 3$ eV, and oxygen $J_H = 0.7$ eV), one can immediately see that for the copper chains with 90° geometry, $J^{\mathrm{Cu,direct}} \approx 3\ \mathrm{meV} \ll |J^{\mathrm{Cu,SE}}| \approx 50$ meV—which justifies why the direct copper exchange is typically neglected in such studies. In reality, the FM exchange is actually really small in such copper chains due to the angle along the copper–oxygen–copper bond not being strictly equal to 90°.

A strong suppression of the direct exchange is also observed in CrI_3,[88] which is an experimentally confirmed 2D ferromagnet. CrI_3 is isostructurally identical to MPS_3 compounds when P atoms are removed and has partially-filled t_{2g} shells, just as $MnPS_3$. This might suggest that CrI_3 should predominantly have AFM interactions, just as $MnPS_3$. However, this is not the case because the relative strength of the direct and superexchange mechanisms is different in CrI_3 and $MnPS_3$. In CrI_3, the Cr–I–Cr bond angle is very close to 90°, leading to a strong FM superexchange, while the Cr–Cr distance is relatively large (3.95 Å), giving rise to a very weak AFM direct exchange. Interestingly, due to the larger distances between the magnetic atoms in CrI_3, the third-neighbor exchange is also less relevant.

Doped Systems $(M_{3/4},X_{1/4})PS_3$. Our strategy is to try to induce long-range FM order *via* chemical doping, keeping the two-dimensional structure of the mother compounds intact. In principle, the chemical doping could influence the magnetic exchanges, especially the long-range ones. To this end, we consider doping of the host systems with distinct possible 3d elements. In particular, at low doping concentration, the main exchange couplings are the magnetic exchanges between the host magnetic atoms (J_i^M for $i = 1, 2, 3$) and between the host

https://doi.org/10.1021/acs.jpcc.2c00646
J. Phys. Chem. C 2022, 126, 6791–6802

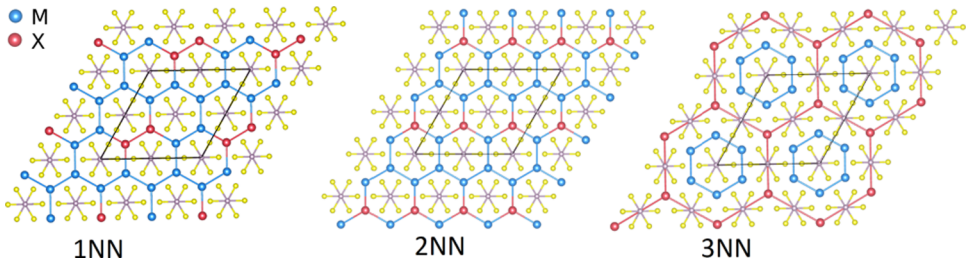

Figure 4. Crystal structure of 2 × 2 supercells consisting of fourfold primitive unit cells. The M and X are the transition metals of the host and dopant atoms, respectively. 1NN, 2NN, and 3NN denote the nearest neighbors, second neighbors, and third neighbors of the dopants, respectively.

impurity atoms (J_i^{MX} for i = 1, 2, 3). Although for most of the 3d doping, the Mn−Mn and the Ni−Ni magnetic couplings remain AFM, in the case of Cr doping, the AFM exchanges between the magnetic atoms of the host turn into FM ones.[89] Thus, we performed DFT + U calculations for 25% concentration of the magnetic dopants (X = Cr, Mn, and Ni) in the hosts of $NiPS_3$ and $MnPS_3$. We have employed various structural arrangements of the atoms (see Figure 4) and collinear spin configurations such as AFM Neel (AFM-N), zigzag (AFM-z), stripy (AFM-s), and FM case. For each of the configurations, the atomic positions have been fully optimized, keeping the lattice constants equal to the pure optimized monolayer structures (see Methods).

Let us first discuss the impact of the dopant on the energetic and structural properties of the hosts. The energy difference between a particular configuration and the magnetic ground state for each considered alloy is presented in Figure 5. Note

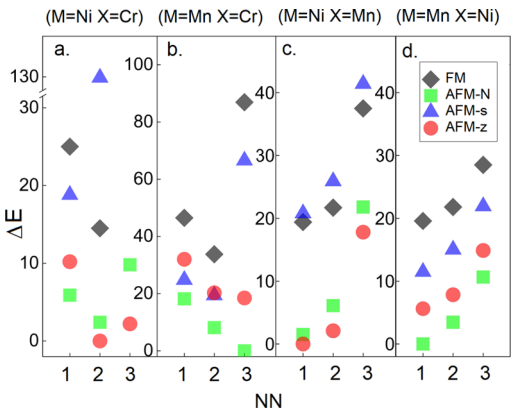

Figure 5. (a−d) Energy difference (ΔE) between a particular magnetic configuration (gray rhombus FM, green square AFM-N, blue triangle AFM-s, and red circle AFM-z) and the magnetic ground state for each of the alloys $(M_{3/4},X_{1/4})PS_3$. Note, that in each of the plots, the most energetically preferable arrangement of the dopants is at the lowest energy. The energy is given in eV per magnetic atom for various structural arrangements of the dopant in the host (1NN, 2NN, and 3NN).

that each of the employed alloys preserves the magnetic ground state of the host, independent of the structural arrangement of the impurity and the type of the dopants (see Figure 5). In addition, the favorite Mn and Ni dopant position is at 1NN (see Figure 5c,d), whereas the Cr dopants prefer to lie further apart, in particular, at 2NN (see Figure 5a) and 3NN (see Figure 5b) structural positions for $NiPS_3$ and $MnPS_3$ hosts, respectively. This reveals that the Mn and Ni dopants have tendency to cluster, while the Cr ions prefer to spread over the host. From now on, we only discuss the magnetic ground-state configurations of the alloys (the one which exhibits the lowest energy in Figure 6 for particular alloy). The magnetization and the band gaps of these systems are collected in Table 2. All considered alloys exhibit a semiconducting behavior (see Table 2). However, only $(Ni_{3/4},Cr_{1/4})PS_3$ and $(Ni_{3/4},Mn_{1/4})PS_3$ alloys have a nonzero net magnetization. Thus, we focus our discussion on these two ferrimagnetic systems. Owing to the different spins of the host and dopant atoms and particular arrangement of the dopants in the $NiPS_3$ host, the ferrimagnetic state appears in these systems. The band structure and the orbital projections of these two ferrimagnetic alloys are presented in Figure 6. Note that in the $(Ni_{3/4},Cr_{1/4})PS_3$ case, bands close to the Fermi level are mainly composed of 3d states of Cr dopants, causing a sizeable reduction in the energy gap compared to pure $NiPS_3$ (2.3 eV for U = 6 eV). In the case of Mn impurities, the valence band maximum is mainly composed of Mn 3d states, whereas the conduction band minimum consists of very flat bands of Ni atoms (see Figure 6b).

Next, we examine the mixed exchange couplings between the metal atom of the host and the impurity J_i^{MX} within the classical Ising Hamiltonian in the honeycomb lattice for the smallest possible cell containing 25% dopant concentration (for details see Supporting Information and Figure S1 therein). Note that the FM exchange couplings are obtained for the Mn and Ni nearest neighbors and Cr−Cr ions at the second-nearest-neighbor distance (see J_2^X in Table 3). The similar results for Cr have been recently reported in ref 90. In addition, the different values for J_1^{MnNi} (−1 meV) and J_1^{NiMn} (−0.7 meV) stems from the different lattice parameters of the hosts (see Table 3). Although the mixed exchange coupling obtained for $(Ni_{3/4},Mn_{1/4})PS_3$ correctly reflected the 1NN AFM-z ground-state configuration for this system, the difference between the 1NN AFM-N and 1NN AFM-z is just 1.5 meV per magnetic ion (see Figure 5c), thus resulting in magnetic frustration between the Mn and Ni atoms at the honeycomb sites due to the competition between the Néel and zigzag configurations, similar to the results reported in ref 35. Moreover, the critical temperature is directly related to the strength of the exchange couplings. Generally, the mixed exchange couplings are smaller than those in the corresponding metal atoms of the hosts. Thus, the critical temperature of the mixed structure is expected to be smaller than that for the corresponding pure system, which is in line with recent experimental reports on the $Ni_{1-x}Mn_xPS_3$ alloy[35] and with series of the mixed-system studies, where the suppression of T_N temperature with dopant substitution is reported.[27,29,34] In addition, one should expect the further reduction of T_N temperature of the employed mixed systems due to the

https://doi.org/10.1021/acs.jpcc.2c00646
J. Phys. Chem. C 2022, 126, 6791−6802

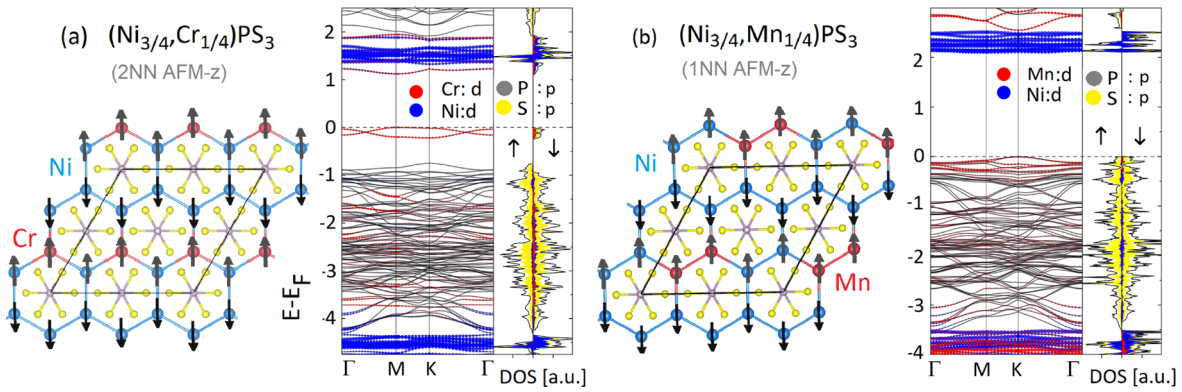

Figure 6. Band structure and projected density of states (PDOS) for 2D ferrimagnetic alloys: (a) $(Ni_{3/4},Cr_{1/4})PS_3$ and (b) $(Ni_{3/4},Mn_{1/4})PS_3$. On the left side of (a,b), the corresponding atomic structural arrangements and local spin magnetic configurations are presented. Note that the spin of the dopant and the host atoms has different magnitudes, which are not visible here (spin arrows are not in scale). For better visibility, the spin channels and projections of the p states of S and P atoms are presented only in PDOS. The energy is given in eV, and the Fermi level is placed at zero.

Table 2. Results for the Most Energetically Favorable Position of the Dopants in the $(M_{3/4},X_{1/4})$ Alloys[a]

alloy $(M_{3/4},X_{1/4})PS_3$	magn. state (2 × 2) sc	M [μ_B] per sc	band gap [eV]
$(Mn_{3/4},Cr_{1/4})PS_3$	3NN AFM-N	0	1.7 (D, Γ)
$(Mn_{3/4},Ni_{1/4})PS_3$	1NN AFM-N	0	2.16 (D at K)
$(Ni_{3/4},Cr_{1/4})PS_3$	2NN AFM-z	3.9	1.1 (↑, D) 2.11 (↓, ID)
$(Ni_{3/4},Mn_{1/4})PS_3$	1NN AFM-z	5.7	2.11 (for both spins)

[a]M is the total magnetization of the cell.

Table 3. Exchange Coupling Strengths J_i Calculated for Various Alloy Systems, Implied by the Ising Model[a]

$(M_{0.75},X_{0.25})PS_3$	J_1^{XM}	J_2^{XM}	J_2^{X}	J_3^{XM}
$(Mn_{3/4},Cr_{1/4})PS_3$	2.5	0.1	−1.1	−0.4
$(Mn_{3/4},Ni_{1/4})PS_3$	−0.7	−0.5	−0.6	2.0
$(Ni_{3/4},Mn_{1/4})PS_3$	−1.0	0.3	0.15	4.9
$(Ni_{3/4},Cr_{1/4})PS_3$	2.2	0.4	−0.3	2.3

[a]Positive and negative J_i indicate AFM and FM ordering, respectively.

possible disorder of the dopant atoms in the host, as reported in refs 30 and 34, which is not accounted in our studies.

CONCLUSIONS

First, we examined the magnetic and electronic properties of the AFM-ordered systems $MnPS_3$ and $NiPS_3$ (without magnetic impurities). We presented a qualitative explanation for the relative ratio of the different nearest neighbor (first, second, and third neighbor) exchange couplings by studying an effective direct exchange for both $MnPS_3$ and $NiPS_3$. In particular, we demonstrated that the third-neighbor exchange dominates in $NiPS_3$ due to the filling of the t_{2g} subshell, whereas for $MnPS_3$, the first-neighbor exchange is prevailed, owing to the presence of the t_{2g} magnetism.

We showed in this work that the onset of the nearest-neighbor FM coupling in $NiPS_3$ is due to the relatively strong (FM) superexchange, which is enabled by the complete filling of the t_{2g} shell and by the (close to) 90° nickel−sulfur−nickel nearest neighbor bond. Nevertheless, even these relatively "fortunate" circumstances do not guarantee that the strong further neighbor exchange can also be FM. The reason for this lies in the further neighbor bonds, which are no longer of a "90° variety"—and the latter bonds are, apart from specific Jahn−Teller effects, the only way to obtain FM couplings in Mott insulators. From a more general perspective, this study confirms the paradigm that the AFM couplings are natural to the Mott insulating compounds.

Second, we examined the properties of the $MnPS_3$ and $NiPS_3$ compounds doped with 25% impurities (Ni in $MnPS_3$, Mn in $NiPS_3$, and Cr in both hosts). It turned out that all of the investigated alloys are Mott insulating, albeit with generally smaller band gaps than those of the corresponding host. Crucially, we demonstrated an extreme robustness of the AFM phases against impurity doping of the $MnPS_3$ and $NiPS_3$ compounds. Hence, ferromagnetism cannot be easily stabilized by impurity doping, in agreement with the above paradigm. Nevertheless, as the dopants have different spins than the pure phases, the alloys exhibit ferrimagnetic properties for particular arrangements of dopants.

The Mn and Ni impurities prefer to form dimers within the host, whereas the Cr dopants prefer to be further apart. Interestingly, unlike for the hosts, the first and second (dopant−host) exchange couplings are of similar order of magnitude. The latter leads to frustration in the case of AFM couplings. We suggest that this may be one of the reasons of the observed lower magnetic ordering temperature of the doped systems.[35]

Our work sheds light on the origin of magnetism in the AFM family of transition metal phosphorus trichalcogenides by pointing out the mechanisms which govern the benchmark compounds, thus extending the fundamental knowledge of 2D magnetism.

ASSOCIATED CONTENT

Supporting Information

The Supporting Information is available free of charge at https://pubs.acs.org/doi/10.1021/acs.jpcc.2c00646.

Exchange interactions calculated within DFT + U and (II) Wannier analysis (PDF)

AUTHOR INFORMATION

Corresponding Author

Magdalena Birowska − *Faculty of Physics, University of Warsaw, PL-02093 Warsaw, Poland;* orcid.org/0000-0001-6357-7913; Email: birowska@fuw.edu.pl

https://doi.org/10.1021/acs.jpcc.2c00646
J. Phys. Chem. C 2022, 126, 6791−6802

Authors

Carmine Autieri − *International Research Centre Magtop, Institute of Physics, Polish Academy of Sciences, PL-02668 Warsaw, Poland; Consiglio Nazionale delle Ricerche CNR-SPIN, UOS Salerno, I-84084 Fisciano, Salerno, Italy*

Giuseppe Cuono − *International Research Centre Magtop, Institute of Physics, Polish Academy of Sciences, PL-02668 Warsaw, Poland*

Canio Noce − *Dipartimento di Fisica "E.R. Caianiello", Università degli Studi di Salerno, I-84084 Fisciano, Salerno, Italy; Consiglio Nazionale delle Ricerche CNR-SPIN, UOS Salerno, I-84084 Fisciano, Salerno, Italy*

Milosz Rybak − *Department of Semiconductor Materials Engineering, Faculty of Fundamental Problems of Technology, Wrocław University of Science and Technology, PL-50370 Wrocław, Poland*

Kamila M. Kotur − *Faculty of Physics, University of Warsaw, PL-02093 Warsaw, Poland*

Cliò Efthimia Agrapidis − *Faculty of Physics, University of Warsaw, PL-02093 Warsaw, Poland;* orcid.org/0000-0003-4778-3156

Krzysztof Wohlfeld − *Faculty of Physics, University of Warsaw, PL-02093 Warsaw, Poland*

Complete contact information is available at: https://pubs.acs.org/10.1021/acs.jpcc.2c00646

Notes

The authors declare no competing financial interest.

■ ACKNOWLEDGMENTS

C.A. and G.C. equally contributed to this work. The authors acknowledge support from the National Science Centre (NCN Poland): M.B. acknowledges support within grant UMO-2016/23/D/ST3/03446, K.W. and C.E.A. acknowledge support within grant UMO-2016/22/E/ST3/00560, K.W. acknowledges support within grant 2016/23/B/ST3/00839 and C.E.A. acknowledges support within grant UMO-2021/40/C/ST3/00177. For the purpose of Open Access, the author has applied a CC-BY public copyright license to any Author Accepted Manuscript (AAM) version arising from this submission. C.A. and G.C. were supported by the Foundation for Polish Science through the International Research Agendas program co-financed by the European Union within the Smart Growth Operational Programme. Access to computing facilities of PL-Grid Polish Infrastructure for Supporting Computational Science in the European Research Space and of the Interdisciplinary Center of Modeling (ICM), University of Warsaw, is gratefully acknowledged, grant nos. G73-23 and G75-10. We acknowledge the CINECA award under the ISCRA initiatives IsC76 "MEPBI" and IsC81 "DISTANCE" grant, for the availability of high-performance computing resources and support. We made use of computing facilities of TU Dresden ZIH within the project "TransPheMat".

■ ADDITIONAL NOTES

[a]The second neighbor coupling is very small and we leave it out from the analysis.

[b]Note that the finite Coulomb repulsion cost on sulfur just renormalizes the (anyway quite hard to estimate) charge transfer energy.

■ REFERENCES

(1) Manzeli, S.; Ovchinnikov, D.; Pasquier, D.; Yazyev, O. V.; Kis, A. 2D transition metal dichalcogenides. *Nat. Rev. Mater.* **2017**, *2*, 17033.

(2) Gibertini, M.; Koperski, M.; Morpurgo, A. F.; Novoselov, K. S. Magnetic 2D materials and heterostructures. *Nat. Nanotechnol.* **2019**, *14*, 408−419.

(3) Huang, B.; Clark, G.; Navarro-Moratalla, E.; Klein, D. R.; Cheng, R.; Seyler, K. L.; Zhong, D.; Schmidgall, E.; McGuire, M. A.; Cobden, D. H.; et al. Layer-dependent ferromagnetism in a van der Waals crystal down to the monolayer limit. *Nature* **2017**, *546*, 270−273.

(4) Gong, C.; Li, L.; Li, Z.; Ji, H.; Stern, A.; Xia, Y.; Cao, T.; Bao, W.; Wang, C.; Wang, Y.; et al. Discovery of intrinsic ferromagnetism in two-dimensional van der Waals crystals. *Nature* **2017**, *546*, 265−269.

(5) Deng, Y.; Yu, Y.; Song, Y.; Zhang, J.; Wang, N. Z.; Sun, Z.; Yi, Y.; Wu, Y. Z.; Wu, S.; Zhu, J.; et al. Gate-tunable room-temperature ferromagnetism in two-dimensional Fe_3GeTe_2. *Nature* **2018**, *563*, 94−99.

(6) Amoroso, D.; Barone, P.; Picozzi, S. Spontaneous skyrmionic lattice from anisotropic symmetric exchange in a Ni-halide monolayer. *Nat. Commun.* **2020**, *11*, 5784.

(7) Du, K.-z.; Wang, X.-z.; Liu, Y.; Hu, P.; Utama, M. I. B.; Gan, C. K.; Xiong, Q.; Kloc, C. Weak Van der Waals Stacking, Wide-Range Band Gap, and Raman Study on Ultrathin Layers of Metal Phosphorus Trichalcogenides. *ACS Nano* **2016**, *10*, 1738−1743.

(8) Lee, J.-U.; Lee, S.; Ryoo, J. H.; Kang, S.; Kim, T. Y.; Kim, P.; Park, C.-H.; Park, J.-G.; Cheong, H. Ising-Type Magnetic Ordering in Atomically Thin $FePS_3$. *Nano Lett.* **2016**, *16*, 7433−7438.

(9) Budniak, A. K.; Zelewski, S. J.; Birowska, M.; Woźniak, T.; Bendikov, T.; Kauffmann, Y.; Amouyal, Y.; Kudrawiec, R.; Lifshitz, E. Spectroscopy and Structural Investigation of Iron Phosphorus Trisulfide—$FePS_3$. *Adv. Opt. Mater.* **2022**, *10*, 2102489.

(10) Birowska, M.; Faria Junior, P. E.; Fabian, J.; Kunstmann, J. Large exciton binding energies in $MnPS_3$ as a case study of a van der Waals layered magnet. *Phys. Rev. B* **2021**, *103*, L121108.

(11) Li, Y.; Wu, X.; Gu, Y.; Le, C.; Qin, S.; Thomale, R.; Hu, J. Topological superconductivity in Ni-based transition metal trichalcogenides. *Phys. Rev. B* **2019**, *100*, 214513.

(12) Kim, H.-S.; Haule, K.; Vanderbilt, D. Mott Metal-Insulator Transitions in Pressurized Layered Trichalcogenides. *Phys. Rev. Lett.* **2019**, *123*, 236401.

(13) Kim, S. Y.; Kim, T. Y.; Sandilands, L. J.; Sinn, S.; Lee, M.-C.; Son, J.; Lee, S.; Choi, K.-Y.; Kim, W.; Park, B.-G.; et al. Charge-Spin Correlation in van der Waals Antiferromagnet $NiPS_3$. *Phys. Rev. Lett.* **2018**, *120*, 136402.

(14) Wang, Y.; Ying, J.; Zhou, Z.; Sun, J.; Wen, T.; Zhou, Y.; Li, N.; Zhang, Q.; Han, F.; Xiao, Y.; et al. Emergent superconductivity in an iron-based honeycomb lattice initiated by pressure-driven spin-crossover. *Nat. Commun.* **2018**, *9*, 1914.

(15) Ho, C.-H.; Hsu, T.-Y.; Muhimmah, L. C. The band-edge excitons observed in few-layer $NiPS_3$. *npj 2D Mater. Appl.* **2021**, *5*, 8.

(16) Belvin, C. A.; Baldini, E.; Ozel, I. O.; Mao, D.; Po, H. C.; Allington, C. J.; Son, S.; Kim, B. H.; Kim, J.; Hwang, I.; et al. Exciton-driven antiferromagnetic metal in a correlated van der Waals insulator. *Nat. Commun.* **2021**, *12*, 4837.

(17) Afanasiev, D.; Hortensius, J. R.; Matthiesen, M.; Mañas-Valero, S.; Šiškins, M.; Lee, M.; Lesne, E.; van der Zant, H. S. J.; Steeneken, P. G.; Ivanov, B. A.; et al. Controlling the anisotropy of a van der Waals antiferromagnet with light. *Sci. Adv.* **2021**, *7*, No. eabf3096.

(18) Němec, P.; Fiebig, M.; Kampfrath, T.; Kimel, A. V. Antiferromagnetic opto-spintronics. *Nat. Phys.* **2018**, *14*, 229−241.

(19) Kampfrath, T.; Sell, A.; Klatt, G.; Pashkin, A.; Mährlein, S.; Dekorsy, T.; Wolf, M.; Fiebig, M.; Leitenstorfer, A.; Huber, R. Coherent terahertz control of antiferromagnetic spin waves. *Nat. Photonics* **2011**, *5*, 31−34.

(20) Kriegner, D.; Výborný, K.; Olejník, K.; Reichlová, H.; Novák, V.; Marti, X.; Gazquez, J.; Saidl, V.; Němec, P.; Volobuev, V. V.; et al. Multiple-stable anisotropic magnetoresistance memory in antiferromagnetic MnTe. *Nat. Commun.* **2016**, *7*, 11623.

(21) Chittari, B. L.; Park, Y.; Lee, D.; Han, M.; MacDonald, A. H.; Hwang, E.; Jung, J. Electronic and magnetic properties of single-layer MPX_3 metal phosphorous trichalcogenides. *Phys. Rev. B* **2016**, *94*, 184428.
(22) Li, X.; Wu, X.; Yang, J. Half-Metallicity in MnPSe3 Exfoliated Nanosheet with Carrier Doping. *J. Am. Chem. Soc.* **2014**, *136*, 11065−11069.
(23) Yang, J.; Zhou, Y.; Dedkov, Y.; Voloshina, E. Dirac Fermions in Half-Metallic Ferromagnetic Mixed $Cr_{1-x}M_xPSe_3$ Monolayers. *Adv. Theory Simul.* **2020**, *3*, 2000228.
(24) Lee, S.; Park, J.; Choi, Y.; Raju, K.; Chen, W.-T.; Sankar, R.; Choi, K.-Y. Chemical tuning of magnetic anisotropy and correlations in $Ni_{1-x}Fe_xPS_3$. *Phys. Rev. B* **2021**, *104*, 174412.
(25) Chandrasekharan, N.; Vasudevan, S. Dilution of a layered antiferromagnet: Magnetism in $Mn_xZn_{1-x}PS_3$. *Phys. Rev. B: Condens. Matter Mater. Phys.* **1996**, *54*, 14903−14906.
(26) Mulders, A. M.; Klaasse, J. C. P.; Goossens, D. J.; Chadwick, J.; Hicks, T. J. High-field magnetization in the diluted quasi-two-dimensional Heisenberg antiferromagnet $Mn_{1-x}Zn_xPS_3$. *J. Phys.: Condens. Matter* **2002**, *14*, 8697−8705.
(27) Masubuchi, T.; Hoya, H.; Watanabe, T.; Takahashi, Y.; Ban, S.; Ohkubo, N.; Takase, K.; Takano, Y. Phase diagram, magnetic properties and specific heat of Mn1−xFexPS3. *J. Alloys Compd.* **2008**, *460*, 668−674.
(28) Goossens, D. J.; Studer, A. J.; Kennedy, S. J.; Hicks, T. J. The impact of magnetic dilution on magnetic order in $MnPS_3$. *J. Phys.: Condens. Matter* **2000**, *12*, 4233−4242.
(29) Goossens, D. J.; Hicks, T. J. The magnetic phase diagram of $MnZnPS_3$. *J. Phys.: Condens. Matter* **1998**, *10*, 7643−7652.
(30) Manríquez, V.; Barahona, P.; Pena, O. Physical properties of the cation-mixed M'MPS_3 phases. *Mater. Res. Bull.* **2000**, *35*, 1889−1895.
(31) Goossens, D. J.; Brazier-Hollins, S.; James, D. R.; Hutchison, W. D.; Hester, J. R. Magnetic structure and glassiness in Fe0.5Ni0.5PS3. *J. Magn. Magn. Mater.* **2013**, *334*, 82−86.
(32) Graham, J. N.; Coak, M. J.; Son, S.; Suard, E.; Park, J.-G.; Clark, L.; Wildes, A. R. Local nuclear and magnetic order in the two-dimensional spin glass $Mn_{0.5}Fe_{0.5}PS_3$. *Phys. Rev. Mater.* **2020**, *4*, 084401.
(33) He, Y.; Dai, Y.-D.; Huang, H.; Lin, J.; Hsia, Y. The ordering distribution of the metal ions in the layered cation-mixed phosphorus trisulfides MnxFe1-xPS3. *J. Alloys Compd.* **2003**, *359*, 41−45.
(34) Bhutani, A.; Zuo, J. L.; McAuliffe, R. D.; dela Cruz, C. R.; Shoemaker, D. P. Strong anisotropy in the mixed antiferromagnetic system $Mn_{1-x}Fe_xPSe_3$. *Phys. Rev. Mater.* **2020**, *4*, 034411.
(35) Basnet, R.; Wegner, A.; Pandey, K.; Storment, S.; Hu, J. Highly sensitive spin-flop transition in antiferromagnetic van der Waals material MPS_3 (M = Ni and Mn). *Phys. Rev. Mater.* **2021**, *5*, 064413.
(36) Joy, P. A.; Vasudevan, S. Magnetism in the layered transition-metal thiophosphates MPS_3 (M=Mn, Fe, and Ni). *Phys. Rev. B: Condens. Matter Mater. Phys.* **1992**, *46*, 5425−5433.
(37) Šiškins, M.; Lee, M.; Mañas-Valero, S.; Coronado, E.; Blanter, Y. M.; van der Zant, H. S. J.; Steeneken, P. G. Magnetic and electronic phase transitions probed by nanomechanical resonators. *Nat. Commun.* **2020**, *11*, 2698.
(38) Long, G.; Henck, H.; Gibertini, M.; Dumcenco, D.; Wang, Z.; Taniguchi, T.; Watanabe, K.; Giannini, E.; Morpurgo, A. F. Persistence of Magnetism in Atomically Thin $MnPS_3$ Crystals. *Nano Lett.* **2020**, *20*, 2452−2459.
(39) Zhong, D.; Seyler, K. L.; Linpeng, X.; Cheng, R.; Sivadas, N.; Huang, B.; Schmidgall, E.; Taniguchi, T.; Watanabe, K.; McGuire, M. A.; Yao, W.; Xiao, D.; Fu, K. C.; Xu, X. Van der Waals engineering of ferromagnetic semiconductor heterostructures for spin and valleytronics. *Sci. Adv.* **2017**, *3*, No. e1603113.
(40) Zener, C. Interaction between the *d*-Shells in the Transition Metals. II. Ferromagnetic Compounds of Manganese with Perovskite Structure. *Phys. Rev.* **1951**, *82*, 403−405.
(41) Vaugier, L.; Jiang, H.; Biermann, S. Hubbard *U* and Hund exchange *J* in transition metal oxides: Screening versus localization trends from constrained random phase approximation. *Phys. Rev. B: Condens. Matter Mater. Phys.* **2012**, *86*, 165105.
(42) Kresse, G.; Hafner, J. Ab initio molecular dynamics for liquid metals. *Phys. Rev. B: Condens. Matter Mater. Phys.* **1993**, *47*, 558−561.
(43) Kresse, G.; Furthmüller, J. Efficiency of ab-initio total energy calculations for metals and semiconductors using a plane-wave basis set. *Comput. Mater. Sci.* **1996**, *6*, 15−50.
(44) Blöchl, P. E. Projector augmented-wave method. *Phys. Rev. B: Condens. Matter Mater. Phys.* **1994**, *50*, 17953−17979.
(45) Kresse, G.; Joubert, D. From ultrasoft pseudopotentials to the projector augmented-wave method. *Phys. Rev. B: Condens. Matter Mater. Phys.* **1999**, *59*, 1758−1775.
(46) Perdew, J. P.; Burke, K.; Ernzerhof, M. Generalized Gradient Approximation Made Simple. *Phys. Rev. Lett.* **1996**, *77*, 3865−3868.
(47) Tawfik, S. A.; Gould, T.; Stampfl, C.; Ford, M. J. Evaluation of van der Waals density functionals for layered materials. *Phys. Rev. Mater.* **2018**, *2*, 034005.
(48) Birowska, M.; Milowska, K.; Majewski, J. A. Van Der Waals Density Functionals for Graphene Layers and Graphite. *Acta Phys. Pol., A* **2011**, *120*, 845−848.
(49) Milowska, K.; Birowska, M.; Majewski, J. A. Mechanical, electrical, and magnetic properties of functionalized carbon nanotubes. *AIP Conf. Proc.* **2011**, *1399*, 827−828.
(50) Birowska, M.; Marchwiany, M. E.; Draxl, C.; Majewski, J. A. Assessment of approaches for dispersive forces employing semi-hydrogenated graphene as a case study. *Comput. Mater. Sci.* **2021**, *186*, 109940.
(51) Grimme, S. Semiempirical GGA-type density functional constructed with a long-range dispersion correction. *J. Comput. Chem.* **2006**, *27*, 1787−1799.
(52) Grimme, S.; Antony, J.; Ehrlich, S.; Krieg, H. A consistent and accurate ab initio parametrization of density functional dispersion correction (DFT-D) for the 94 elements H-Pu. *J. Chem. Phys.* **2010**, *132*, 154104.
(53) Islam, R.; Ghosh, B.; Autieri, C.; Chowdhury, S.; Bansil, A.; Agarwal, A.; Singh, B. Tunable spin polarization and electronic structure of bottom-up synthesized $MoSi_2N_4$ materials. *Phys. Rev. B* **2021**, *104*, L201112.
(54) Dudarev, S. L.; Botton, G. A.; Savrasov, S. Y.; Humphreys, C. J.; Sutton, A. P. Electron-energy-loss spectra and the structural stability of nickel oxide: An LSDA+U study. *Phys. Rev. B: Condens. Matter Mater. Phys.* **1998**, *57*, 1505−1509.
(55) Cococcioni, M.; de Gironcoli, S. Linear response approach to the calculation of the effective interaction parameters in the LDA+U method. *Phys. Rev. B: Condens. Matter Mater. Phys.* **2005**, *71*, 035105.
(56) Wang, L.; Maxisch, T.; Ceder, G. Oxidation energies of transition metal oxides within the GGA + U framework. *Phys. Rev. B: Condens. Matter Mater. Phys.* **2006**, *73*, 195107.
(57) Autieri, C.; Śliwa, C.; Islam, R.; Cuono, G.; Dietl, T. Momentum-resolved spin splitting in Mn-doped trivial CdTe and topological HgTe semiconductors. *Phys. Rev. B* **2021**, *103*, 115209.
(58) Ivanov, S. A.; Bush, A. A.; Stash, A. I.; Kamentsev, K. E.; Shkuratov, V. Y.; Kvashnin, Y. O.; Autieri, C.; Di Marco, I.; Sanyal, B.; Eriksson, O.; et al. Polar Order and Frustrated Antiferromagnetism in Perovskite Pb2MnWO6 Single Crystals. *Inorg. Chem.* **2016**, *55*, 2791−2805.
(59) Mostofi, A. A.; Yates, J. R.; Lee, Y.-S.; Souza, I.; Vanderbilt, D.; Marzari, N. wannier90: A tool for obtaining maximally-localised Wannier functions. *Comput. Phys. Commun.* **2008**, *178*, 685−699.
(60) Pizzi, G.; et al. Wannier90 as a community code: new features and applications. *J. Phys.: Condens. Matter* **2020**, *32*, 165902.
(61) Autieri, C.; Sanyal, B. Unusual ferromagnetic $YMnO_3$ phase in $YMnO_3/La_{2/3}Sr_{1/3}MnO_3$ heterostructures. *New J. Phys.* **2014**, *16*, 113031.
(62) Cuono, G.; Autieri, C.; Forte, F.; Mercaldo, M. T.; Romano, A.; Avella, A.; Noce, C. A minimal tight-binding model for the quasi-one-dimensional superconductor $K_2Cr_3As_3$. *New J. Phys.* **2019**, *21*, 063027.
(63) van Thiel, T. C.; Brzezicki, W.; Autieri, C.; Hortensius, J. R.; Afanasiev, D.; Gauquelin, N.; Jannis, D.; Janssen, N.; Groenendijk, D.

https://doi.org/10.1021/acs.jpcc.2c00646
J. Phys. Chem. C 2022, 126, 6791−6802

J.; Fatermans, J.; et al. Coupling Charge and Topological Reconstructions at Polar Oxide Interfaces. *Phys. Rev. Lett.* **2021**, *127*, 127202.
(64) Wildes, A. R.; Roessli, B.; Lebech, B.; Godfrey, K. W. Spin waves and the critical behaviour of the magnetization in. *J. Phys.: Condens. Matter* **1998**, *10*, 6417−6428.
(65) Lançon, D.; Ewings, R. A.; Guidi, T.; Formisano, F.; Wildes, A. R. Magnetic exchange parameters and anisotropy of the quasi-two-dimensional antiferromagnet $NiPS_3$. *Phys. Rev. B* **2018**, *98*, 134414.
(66) Olsen, T. Magnetic anisotropy and exchange interactions of two-dimensional $FePS_3$, $NiPS_3$ and $MnPS_3$ from first principles calculations. *J. Phys. D: Appl. Phys.* **2021**, *54*, 314001.
(67) Sivadas, N.; Daniels, M. W.; Swendsen, R. H.; Okamoto, S.; Xiao, D. Magnetic ground state of semiconducting transition-metal trichalcogenide monolayers. *Phys. Rev. B: Condens. Matter Mater. Phys.* **2015**, *91*, 235425.
(68) Ressouche, E.; Loire, M.; Simonet, V.; Ballou, R.; Stunault, A.; Wildes, A. Magnetoelectric $MnPS_3$ as a candidate for ferrotoroidicity. *Phys. Rev. B: Condens. Matter Mater. Phys.* **2010**, *82*, 100408.
(69) Hicks, T. J.; Keller, T.; Wildes, A. R. Magnetic dipole splitting of magnon bands in a two dimensional antiferromagnet. *J. Magn. Magn. Mater.* **2019**, *474*, 512−516.
(70) Cleary, D. A.; Francis, A. H.; Lifshitz, E. Analysis of the ESR spectrum of manganese (II) in the layered compound $Cd_2P_2Se_6$. *Chem. Phys.* **1986**, *106*, 123−129.
(71) Wildes, A. R.; Rønnow, H. M.; Roessli, B.; Harris, M. J.; Godfrey, K. W. Anisotropy and the critical behaviour of the quasi-2D antiferromagnet, $MnPS_3$. *J. Magn. Magn. Mater.* **2007**, *310*, 1221−1223.
(72) Kim, K.; Lim, S. Y.; Lee, J.-U.; Lee, S.; Kim, T. Y.; Park, K.; Jeon, G. S.; Park, C.-H.; Park, J.-G.; Cheong, H. Suppression of magnetic ordering in XXZ-type antiferromagnetic monolayer $NiPS_3$. *Nat. Commun.* **2019**, *10*, 345.
(73) Kim, T. Y.; Park, C.-H. Magnetic Anisotropy and Magnetic Ordering of Transition-Metal Phosphorus Trisulfides. *Nano Lett.* **2021**, *21*, 10114−10121.
(74) Ni, Z.; Zhang, H.; Hopper, D. A.; Haglund, A. V.; Huang, N.; Jariwala, D.; Bassett, L. C.; Mandrus, D. G.; Mele, E. J.; Kane, C. L.; et al. Direct Imaging of Antiferromagnetic Domains and Anomalous Layer-Dependent Mirror Symmetry Breaking in Atomically Thin $MnPS_3$. *Phys. Rev. Lett.* **2021**, *127*, 187201.
(75) Koo, H.-J.; Kremer, R.; Whangbo, M.-H. Unusual Spin Exchanges Mediated by the Molecular Anion P2S64: Theoretical Analyses of the Magnetic Ground States, Magnetic Anisotropy and Spin Exchanges of MPS3 (M = Mn, Fe, Co, Ni). *Molecules* **2021**, *26*, 1410.
(76) Yang, J.; Zhou, Y.; Guo, Q.; Dedkov, Y.; Voloshina, E. Electronic, magnetic and optical properties of $MnPX_3$ (X = S, Se) monolayers with and without chalcogen defects: a first-principles study. *RSC Adv.* **2020**, *10*, 851.
(77) Wu, Z.; Xu, S.; Zhou, Y.; Guo, Q.; Dedkov, Y.; Voloshina, E. Adsorption of Water Molecules on Pristine and Defective $NiPX_3$ (X: S, Se) Monolayers. *Adv. Theory Simul.* **2021**, *4*, 2100182.
(78) Goodenough, J. B. Theory of the Role of Covalence in the Perovskite-Type Manganites [La, *M*(II)]MnO_3. *Phys. Rev.* **1955**, *100*, 564−573.
(79) Kanamori, J. Superexchange interaction and symmetry properties of electron orbitals. *J. Phys. Chem. Solids* **1959**, *10*, 87−98.
(80) Pavarini, E.; Koch, E.; Anders, F.; Jarrell, M. Correlated Electrons: From Models to Materials. *Forschungszent. Juelich* **2012**, *2*, 7.1−7.31.
(81) Autieri, C.; Koch, E.; Pavarini, E. Mechanism of structural phase transitions in $KCrF_3$. *Phys. Rev. B: Condens. Matter Mater. Phys.* **2014**, *89*, 155109.
(82) Autieri, C.; Bouhon, A.; Sanyal, B. Gap opening and large spin−orbit splitting in (M = Mo,W; X = S,Se,Te) from the interplay between crystal field and hybridisations: insights from ab-initio theory. *Philos. Mag.* **2017**, *97*, 3381−3395.
(83) Anisimov, V. I.; Solovyev, I. V.; Korotin, M. A.; Czyżyk, M. T.; Sawatzky, G. A. Density-functional theory and NiO photoemission spectra. *Phys. Rev. B: Condens. Matter Mater. Phys.* **1993**, *48*, 16929−16934.
(84) Ushakov, A. V.; Kukusta, D. A.; Yaresko, A. N.; Khomskii, D. I. Magnetism of layered chromium sulfides $MCrS_2$ (*M* = Li, Na, K, Ag, and Au): A first-principles study. *Phys. Rev. B: Condens. Matter Mater. Phys.* **2013**, *87*, 014418.
(85) Slater, J. C.; Koster, G. F. Simplified LCAO Method for the Periodic Potential Problem. *Phys. Rev.* **1954**, *94*, 1498−1524.
(86) Johnston, S.; Monney, C.; Bisogni, V.; Zhou, K.-J.; Kraus, R.; Behr, G.; Strocov, V. N.; Málek, J.; Drechsler, S.-L.; Geck, J.; et al. Electron-lattice interactions strongly renormalize the charge-transfer energy in the spin-chain cuprate Li_2CuO_2. *Nat. Commun.* **2016**, *7*, 10563.
(87) Rosner, H. Electronic structure and exchange integrals of low-dimensional cuprates. Doctoral Thesis, Technische Universitaet Dresden, Dresden, 1999.
(88) Jiang, X.; Liu, Q.; Xing, J.; Liu, N.; Guo, Y.; Liu, Z.; Zhao, J. Recent progress on 2D magnets: Fundamental mechanism, structural design and modification. *Appl. Phys. Rev.* **2021**, *8*, 031305.
(89) Son, J.; Son, S.; Park, P.; Kim, M.; Tao, Z.; Oh, J.; Lee, T.; Lee, S.; Kim, J.; Zhang, K.; et al. Air-Stable and Layer-Dependent Ferromagnetism in Atomically Thin van der Waals CrP_4. *ACS Nano* **2021**, *15*, 16904−16912.
(90) Xu, S.; Wu, Z.; Dedkov, Y.; Voloshina, E. Adsorption of water on the pristine and defective semiconducting 2D $CrPX_3$ monolayers (X: S, Se). *J. Phys.: Condens. Matter* **2021**, *33*, 354001.

https://doi.org/10.1021/acs.jpcc.2c00646
J. Phys. Chem. C 2022, 126, 6791−6802